Technical Note: Identifying biomass burning emissions during ASIA-

2 AQ using greenhouse gas enhancement ratios

- 3 Jason A. Miech^{1,2}, Joshua P. DiGangi¹, Glenn S. Diskin¹, Yonghoon Choi^{1,3}, Richard H. Moore¹, Luke
- 4 D. Ziemba¹, Francesca Gallo^{1,3}, Carolyn E. Jordan^{1,3}, Michael A. Shook¹, Elizabeth B. Wiggins¹, Edward
- 5 L. Winstead^{1,3}, Sayantee Roy^{1,2}, Young Ro Lee⁴, Katherine Ball⁴, John D. Crounse⁴, Paul Wennberg⁴,
- 6 Felix Piel⁵, Stefan Swift⁶, Wojciech Wojnowski^{5,7}, Armin Wisthaler^{5,6}
- 7 NASA Langley Research Center, Hampton, 23666, USA
- 8 ²Oak Ridge Associated Universities, Oak Ridge, 37831-0117, USA
- 9 ³Analytical Mechanics Associates, Hampton, 23666, USA
- 10 ⁴California Institute of Technology, Pasadena, 91125, USA
- ⁵Department of Chemistry, University of Oslo, Oslo, 0313, Norway
- 12 6Institute for Ion Physics and Applied Physics, University of Innsbruck, Innsbruck, 6020, Austria
- 13 ⁷Gdańsk University of Technology, Gdańsk, 80-233, Poland
- 14 Correspondence to: Jason A. Miech (jason.a.miech@nasa.gov)
- 15 Abstract. Biomass burning (BB) is a primary source of atmospheric chemistry reactants, aerosols, and greenhouse gases.
- 16 Smoke plumes have air quality impacts local to the fire itself and regionally via long distance transport. Open burning of
- 17 agriculture fields in Southeast Asia leads to frequent seasonal occurrences of regional BB-induced smoke haze and long-range
- 18 transport of BB particles via the northeast monsoon. The Airborne and Satellite Investigation of Asian Air Quality (ASIA-AQ)
- 19 campaign visited several areas including the Philippines, South Korea, Thailand, and Taiwan during a time of agricultural
- 20 burning. This campaign consisted of airborne measurements on the NASA DC-8 aircraft aimed to validate observations from
- 21 South Korea's Geostationary Environment Monitoring Spectrometer (GEMS) and to address local air quality challenges. We
- 22 developed a method that used a combination of BB markers to identify ASIA-AQ DC-8 data influenced by BB and flag them
- 23 for further analysis. Specifically, we used rolling slope enhancement ratios of CO/CO₂ and CH₄/CO along with mixing ratios
- 24 of CH₃CN, HCN, and CO, and particle scattering coefficient measurements. The flag was triggered when a combination of
- 25 these variables exceeded a flight specific threshold. We found varying levels of BB-influence in the areas studied, with data
- 26 flagged for BB being <1% for the Philippines and Korea, and <2% for Taiwan, but 19% for Thailand. Our method for flagging
- 27 ASIA-AQ BB-affected data can be used to focus additional analyses of the ASIA-AQ campaign such as pairing with back-
- 28 trajectories, satellite hotspot products, and microphysical aerosol characteristics.

9 1 Introduction

- 30 As Asian economies and populations continue to grow, so will their contribution to global greenhouse gas (GHG) emissions,
- 31 driven primarily by increases in fossil fuel combustion and seasonally by biomass burning (BB) events. Left unchecked, these
- 32 emissions will negatively impact air quality and climate, and therefore it is imperative that emission sources are properly
- 33 identified and accounted for in emission inventories. Sources of carbon monoxide (CO) can include: domestic (residential

34 heating and cooking), industrial, and transport sectors; for methane (CH₄) can include: fossil fuels (coal mining), agricultural 35 emissions (enteric fermentation and rice cultivation), and solid waste disposal and wastewater treatment; and for carbon 36 dioxide (CO₂): fossil fuel/biofuel combustion processes (powerplants and transportation) and industrial processes (cement production) (Kurokawa et al., 2013; Kurokawa and Ohara, 2020). Carbon monoxide (CO), while not a greenhouse gas is also 37 38 emitted from urban sources such as domestic (residential heating and cooking), industrial, and transport sectors (Kurokawa et 39 al., 2013; Kurokawa and Ohara, 2020). Biomass burning is also a significant source of these GHGs and CO; however, the seasonal nature of crop residue burning, and unpredictability of natural fires makes it difficult to accurately quantify these 40 41 variables sources (Akagi et al., 2011; Streets et al., 2003; Crutzen and Andreae, 1990). The Airborne and Satellite Investigation of Asian Air Quality (ASIA-AQ) field campaign was conducted during February-42 43 March 2024 near the maximum period of seasonal agricultural burning in Southeast Asia, providing an ideal opportunity to further study biomass burning. ASIA-AQ was an international joint air quality campaign between the National Aeronautics 44 45 and Space Administration (NASA) and several space and environmental agencies in Korea (National Institute of Environmental Research (NIER) and Korea Meteorological Administration (KMA)), the Philippines (Department of 46 Environment and Natural Resources (DENR), Philippine Space Agency (PhilSA), and Manila Observatory), Thailand (Geo-47 Informatics and Space Technology Development Agency (GISTDA) and Pollution Control Department (PCD)), and Taiwan 48 (Ministry of Environment, National Central University (NCU), and Academia Sinica), Observations included in-situ 49 50 measurements of trace gasses, aerosol properties, radiation fluxes, and meteorological parameters from NASA's DC-8 aircraft and several Korean aircraft, remote sensing measurements from NASA's G-III aircraft, satellite observations from Korea's 51 52. GEMS instrument, and several ground station measurements. 53 Current observation-based (top-down) techniques for GHG source apportionment include aircraft-based mass balances 54 (Cambaliza et al., 2015), standard eddy covariance (Helfter et al., 2016), positive matrix factorization (Guha et al., 2015), and 55 isotopic signatures (Fiehn et al., 2023). Enhancement ratios between GHGs have also been used to characterize sources of BB plumes (Akagi et al., 2011; Andreae and Merlet, 2001; Nara et al., 2017; Yokelson et al., 1996); however, Yokelson et al. 56 57 (2013) pointed out several issues with this technique including problems that arise when background concentrations are changing over the measurement period. Halliday et al. (2019) used short-term $\Delta CO/\Delta CO_2$ calculated over 60s rolling windows 58 59 and filtered data by the coefficient of determination (R2) to negate the need for a consistent background measurement. DiGangi et al. (2021) applied a similar method to data from NASA's Atmospheric Carbon Transport-America (ACT-America) 60 campaign to characterize local CO₂ emissions. (DiGangi et al., (2025) adapted this method for use with CH₄/CO ratios for 61 NASA's Cloud, Aerosol, and Monsoon Processes Philippines Experiment (CAMP2EX) airborne field campaign in a chemical 62 63 influence flag, with a focus on separating BB and urban influences. Previous work during the Fire Influence on Regional to Global Environments and Air Quality (FIREX-AQ) airborne campaign used CO and black carbon (BC) enhancements to identify and flag smoke plumes (Warneke et al., 2023). Since the ASIA-AQ campaign overflew many urban areas, a more BB-65 66 specific approach was required. The method presented in this work combines the use of CO/CO2 and CH4/CO ratios to further 67 constrain source contributions. To specifically target BB sources, we have also incorporated mixing ratios of acetonitrile

- (CH₃CN) (Yokelson et al., 2009; Lobert et al., 1990; Holzinger et al., 1999), hydrogen cyanide (HCN) (Yokelson et al., 2009;
- Lobert et al., 1990; Holzinger et al., 1999), CO mixing ratio (Lin et al., 2013; Nara et al., 2017), and aerosol scattering 69
- 70 coefficient (Lin et al., 2013; Tsay et al., 2013) into our method. This work provides a targeted method to identify air masses
- 71 influenced by biomass burning during the 2024 ASIA-AQ airborne field campaign, an example of which is shown in our
- 72 Thailand case study.

2 Data and Methods

91

93

2.1 ASIA-AQ Field Campaign and In Situ Aircraft Measurements

- These methods were developed for the ASIA-AQ campaign, which was a joint international field study focused on air quality 75 challenges local to its areas of study, which included the Philippines, Korea, Thailand, and Taiwan. Data for this campaign 76
- 77 were collected from aircraft, including NASA's DC-8 and G-III and three Korean aircraft, and several ground sites. Sixteen
- DC-8 science flights were conducted between 6 February 2024 and 27 March 2024; the full flight break-down can be found 78
- 79 in Table S1 along with typical flight paths in Figures S1-4. The NASA DC-8 aircraft carried a variety of instruments used for
- in-situ gas-phase, aerosol, radiation, and meteorological measurements. CO2 was measured via non-dispersive infrared 80
- 81 spectroscopy using a modified LICOR 7000 instrument with an uncertainty of 0.25 ppm at <500 ppm and 2% at > 500 ppm
- (Vay et al., 2003). CH4 and CO were measured via wavelength modulation spectroscopy using the Differential Absorption 82
- 83 Carbon monoxide Measurement (DACOM) instrument, with CO uncertainties of 2% for < 1 ppm and 5% for > 1 ppm and
- 84 CH₄ uncertainty of 1% (Sachse et al., 1987, 1991). HCN mixing ratios were measured using a Chemical Ionization High
- Resolution Time of Flight Mass Spectrometer with an uncertainty of 25% plus 35 pptv (CIT-CIMS) (Crounse et al., 2006). 85
- CH₃CN measurements were taken using a Proton-Transfer-Reaction Time-of-Flight Mass Spectrometer (PTR-MS) with an 86
- uncertainty of 13% (Müller et al., 2016; Reinecke et al., 2023). Total aerosol scattering at 550 nm measurements were measured 87
- 88 using a TSI-3563 Nephelometer with an estimated accuracy of 20% and estimated precision of 1 Mm⁻¹ (Anderson and Ogren, 1998). Accumulation-mode aerosol BC mass concentrations were measured by a Single Particle Soot Photometer (SP2-D) 89
- 90 (Droplet Measurement Technologies Inc. (DMT), Longmont, Colorado, USA) with an uncertainty of 20%, operated by NASA
- Langley Research Center. Optical particle size distributions for particles with diameters between 63.1 and 1000 nm were
- 92 measured using a DMT Ultra High Sensitivity Aerosol Spectrometer (UHSAS) Model UHSAS-0.055 (DMT, Longmont
- Colorado USA) with an uncertainty of 20%, while particles with diameters between 3.16 and 89.1 nm were sized using a 94 Scanning Mobility Particle Sizer (SMPS) with an uncertainty of 20%. Submicron particle number concentrations (>10 nm)
- 95 were measured with a TSI Condensation Particle Counter (CPC) CPC-3772 (TSI Inc., Shoreview, Minnesota, USA) with an
- uncertainty of 10%. A duplicate instrument also with 10% uncertainty was used to measure non-volatile particle number 96
- 97 concentrations (>10 nm) with the sample passing through a thermal denuder heated to 350 °C prior to entering the instrument.
- 98 All DC-8 data used in this work had a time resolution of 1 Hz, with the exceptions of the SMPS which measured every minute.
- Hourly Thai precipitation measurements were obtained from the Thailand Pollution Control Department using the Phaya Thai, 99

100 Khet Phaya Thai, and Bangkok sites. This data and the developed BB flag are publicly available on the ASIA-AQ data archive

101 (ASIA-AQ Science Team, 2024).

2.2 Rolling Slope Method

The rolling slope calculation method employed here was taken from Halliday et al. (2019), where linear fits over 120s rolling 103 104 windows of CO vs. CO2 and CH4 vs. CO were calculated using error adjusted bivariate regression as detailed in York et al. 105 (2004) and Cantrell (2008). Applying this method, a maximum of 121 observations were used in each calculation, while the 106 minimum for a valid calculation was set at three. Slopes with low goodness of fit ($R^2 < 0.5$) were filtered out as uncorrelated, 107 and, slopes with a ΔCH_4 , ΔCO , or ΔCO_2 less than five times the precision value were dropped. While Halliday et al. (2019) 108 demonstrated that the shapes of the slope distributions are somewhat insensitive to the R^2 cutoff (when $R^2 > 0.5$), here we 109 observed differences between correlated slopes ($R^2 \ge 0.5$) and uncorrelated slopes ($R^2 < 0.5$). Halliday et al. (2019) also showed 110 that varying the window width did not drastically change the slope distributions. Similarly, Figures S5-7 show that with 111 increasing window width, the number of correlated slopes increases and with an increasing R² cutoff the number decreases; 112 however, the shapes of the slope distributions are similar. Table S2 exhibits the percentage of calculated $\Delta CO/\Delta CO_2$ and 113 ΔCH₄/ΔCO slopes that were correlated for each flight. On average across all flights, 52% of ΔCO/ΔCO₂ slopes and 53% of $\Delta CH_4/\Delta CO$ slopes were correlated according to the $R^2 \ge 0.5$ criterion, in 120s rolling windows. 114

115

127

102

116 ΔCO/ΔCO₂ rolling slopes can be used to isolate plumes or air mass boundaries with correlated behavior and provide a 117 rudimentary source classification. The combustion efficiency of the source is inversely related to the ΔCO/ΔCO₂ slope, 118 therefore we have divided up source behaviors into four combustion efficiency bins based on $\Delta CO/\Delta CO_2$ slopes: 0-1%, 1-2%, 119 2-4%, and >4%, as previously used by Halliday et al., (2019). In this work, the >4% combustion efficiency bin is most relevant 120 for identifying BB-influenced plumes, Figure 1A shows an example of this classification applied to the CO and CO₂ bulk 121 ratios from Thailand Flight 1 demonstrating the ability of this method to highlight different air mass behaviors. $\Delta CH_4/\Delta CO$ 122 slopes have been used to distinguish between urban sources of methane and biomass burning (DiGangi et al., 2025; Reid et 123 al., 2023), with higher slopes indicative of more urban sources and smaller slopes 0<x<~40% with biomass burning. Figure 1B displays the application of these regimes to CO and CH₄ bulk ratios. Both Fig. 1A and 1B demonstrate a large influence 124 from slopes indicative of biomass burning, >4% for ΔCO/ΔCO₂ (shown in dark red) and 0<x<~40% for ΔCH₄/ΔCO (shown 125 126 in orange).

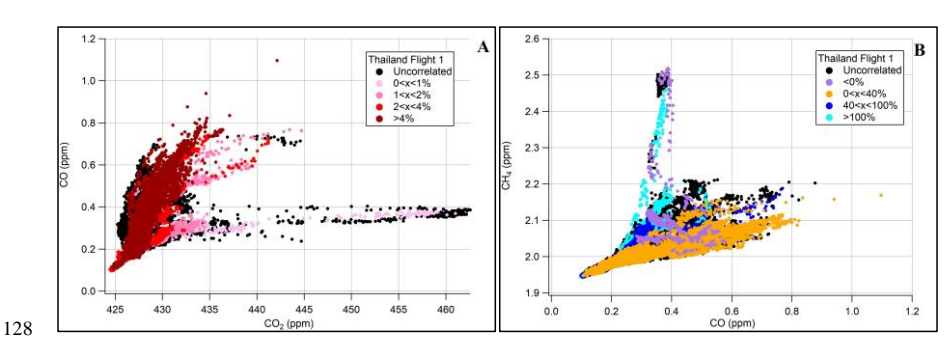


Figure 1. CO vs CO₂ mixing ratios colored by Δ CO/ Δ CO₂ rolling slope enhancement ratio regimes (A) and CH₄ vs CO mixing ratios colored by Δ CH₄/ Δ CO rolling slope enhancement ratio regimes (B) for Thailand flight 1.

2.3 Biomass Burning Flag Determination

The biomass burning flag uses a combination of variables indicative of or a product of biomass burning, including CO mixing ratio, particle scattering at 550 nm, HCN, CH_3CN , $\Delta CO/\Delta CO_2$, and $\Delta CH_4/\Delta CO$. The BB flag is triggered when at least two of the variables meet exceed their flight-specific thresholds, except for $\Delta CH_4/\Delta CO$ which must fall in a range between zero and its threshold (Table S3). Using a single variable was deemed insufficient due to the possibility of confounding factors, for example, the utility of CH_2CN as a BB maker has been shown to be less effective in urban areas due to interference from vehicle and solvent usage emissions (Huangfu et al., 2021). However, when CO mixing ratio and particle scattering are paired together a third variable needs to meet its threshold to trigger the flag; the reasoning for this is to prevent false positives occurring from inefficient combustion processes other than biomass burning, such as transportation and industrial sources. Additionally, the BB flag is triggered when all four non-slope variables are within 10% of their threshold to address edge cases. Example scenarios for triggering the flag are shown in Table 1.

Formatted: Subscript

157

158

159

160

161162

163

164

165

166 167

168

169

170

Table 1. Example securios for triggering the BB flag for Thailand flight 1 ($\frac{2024031603/16/2024}{2024}$). Underlined values in green represent the variables that have exceeded their threshold (χ), italic values in blue are variables within 10% of their threshold (χ). The last row represents an example where all four non-slope variables are at least within 10% of their threshold (χ).

BB Flag	<u>0<</u> ΔCH ₄ /ΔCO <u><</u> x	ΔCO/ΔCO ₂ ≥χ	CO <u>></u> x	HCN≥x	CH ₃ CN≥x	Total scattering @
	(%)	(%)	(ppm)	(ppt)	(ppb)	550 nm <u>≥x</u> (Mm ⁻¹)
Threshold (x)	44.5	4	0.32	2750	1.50	160
✓	N/A	<u>5.1</u>	0.67	<u>2810</u>	1.31	<u>487</u>
✓	40.3	9.8	0.34	1310	0.56	<u>227</u>
×	54.6	2.5	0.22	774	0.30	36
✓	N/A	N/A	0.53	2823	0.91	<u>386</u>
×	N/A	N/A	0.33	1053	0.57	<u> 186</u>
✓	N/A	2.2	0.67	2715	1.43	418

2.3.1 Variable Threshold Determination

The BB flag shares similarities with the Chemical Influence flag developed for CAMP 2 EX, where lower positive Δ CH $_4$ / Δ CO rolling slopes were associated with biomass burning influence (DiGangi et al., 2025; Reid et al., 2023). Here, the specific Δ CH $_4$ / Δ CO cutoff values were chosen on a flight-by-flight basis by evaluating the slope distribution for each flight and looking for distinctive populations. An example of this process is shown in Fig. 2A, where there is a distribution separation occurring at a slope value of 44.5% for the first Thailand flight. For Δ CO/ Δ CO $_2$ the threshold was set to greater than 4% for all flights, as low efficiency processes like biomass burning are associated with higher Δ CO/ Δ CO $_2$ values (Halliday et al., 2019). The thresholds for the other variables were initially determined by identifying at which concentration within the biomass burning regime (as set by Δ CH $_4$ / Δ CO) the variable is distinguishable from non-biomass burning influence regimes. In the Fig. 2B example, that regime is from 0-44.5% Δ CH $_4$ / Δ CO, as determined from Fig. 2A, and the CH $_3$ CN threshold was set to 1.00 ppb. This method was repeated for the other variables (HCN, particle scattering, and CO mixing ratio) and for all flights. Thresholds for the mixing ratio and scattering variables were set on a flight-by-flight basis. Flight specific thresholds were chosen over campaign thresholds due to changing background concentrations, time periods, and environmental conditions for each flight and location.

Formatted: Font: Italic **Formatted Table** Formatted: Font: Italic Formatted: Font: Italic Formatted: Font color: Text 1 Formatted: Font color: Text 1

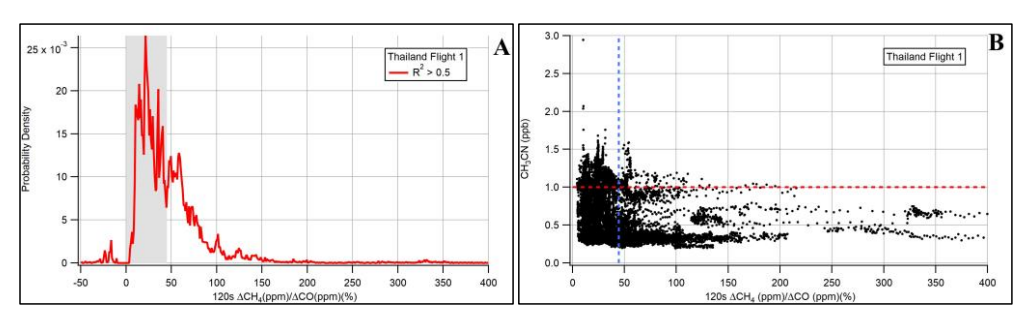


Figure 2 (A) Frequency distribution of rolling slope Δ CH₄/ Δ CO enhancement ratios. The shaded region is the set BB regime for this flight, as determined by the minimum in the distribution. (B) CH₃CN vs Δ CH₄/ Δ CO for Thailand flight 1. The blue vertical line represents the edge of the biomass burning influence regime at 44.5% Δ CH₄/ Δ CO, while the red horizontal line is the preliminary CH₃CN threshold for the BB flag. The upper left quadrant of the figure represents the BB regime.

In the case of thresholds that were more difficult to distinguish, a higher value was initially selected to minimize false positives in the flag. Thresholds were then further refined from this initial value by examining the sensitivity of the total percentage of points flagged to that threshold. The final thresholds were chosen at the lowest levels for which the percentage of points remained essentially constant. Figure 3 demonstrates the results from one of these sensitivity tests performed on the first flight in Thailand. In this case, decreasing the thresholds for CO mixing ratio, CH₃CN, HCN, and particle scattering results in large increases in the number of points flagged. In Fig. 3A, the dashed HCN and CH₃CN traces are still decreasing past their initial threshold values represented by the triangles (2400 ppt and 1.0 ppb); therefore, this is motivation to increase their thresholds by ~15% and ~50% respectively, resulting in the solid traces. The initial thresholds for CO mixing ratio and particle scattering (0.32 ppm and 160), shown as triangles Fig. 3B required no adjustment for this particular flight; the decrease in the percentage of points flagged for the post-adjustment traces is due to the increases in the HCN and CH₃CN thresholds. The final determined thresholds and rolling slope regimes for all flights are in Table S3, while Table 1 provides some example scenarios of the BB flag being triggered or not for Thailand flight 1. The concentration thresholds varied by a factor of 2.6 for CO and up to 8 for CH₃CN, this variability can be explained by changing background concentrations for each flight day and location. This approach was followed to minimize false positives in the dataset; therefore, this method is less sensitive to air masses with only minor influences from biomass burning.

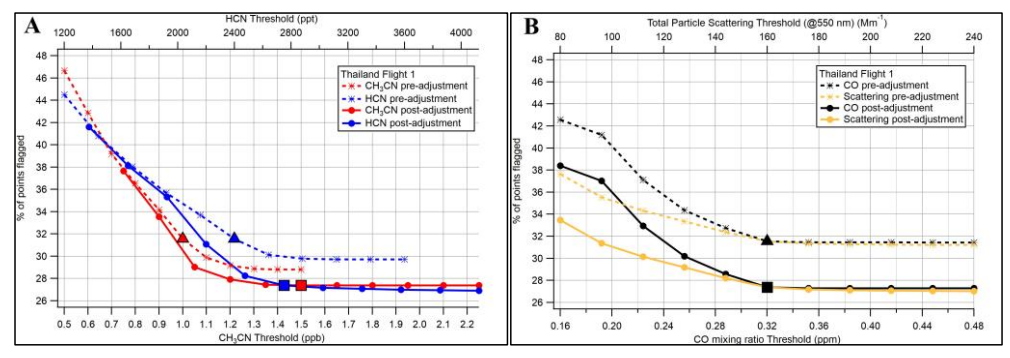


Figure 3. Example variable threshold sensitivity plots for the first Thailand flight. Fig 3A shows the sensitivities for the HCN and CH3CN thresholds established using plots like Fig 2B in the dashed traces and the final thresholds in solid. Fig 3B shows the sensitivities for the CO mixing ratio and total particle scattering thresholds established using plots like Fig 2B in the dashed traces and the final thresholds in solid. The triangles represent the initial thresholds for each variable and the squares the final thresholds.

2.4 HYSPLITHYSPLIT Back_-Trajectories

Air mass history was probed using 48 hour back_trajectories calculated from the DC-8 flight track at one second intervals using NOAA's HYSPLITHYSPLIT model using GFS 0.25° meteorology (Draxler, 1999; Draxler and Hess, 1997, 1998; Stein et al., 2015). For more specific source type, altitude, and receptor location analysis, we used the BB flag as a filter and focused on specific areas and altitudes of the flight path, such as urban areas at low altitudes to determine whether the emissions measured in these locations were local or transport. To empirically quantify these contributions, we totaled the number of back-trajectoryback trajectory points under 1 km that traveled through a certain area prior to ending up at the receptor location; locations used in this analysis are described in Table S4 and shown in Figure S8.

2.5 VIIRS Fire Hotspots & Imagery

The Visible Infrared Imaging Radiometer Suite (VIIRS) I-Band 375 m Active Fire data product was used to assess fire hotspot density over Southeast Asia (Schroeder et al., 2014). Data version 2.0 from the Suomi National Polar-Orbiting Partnership (Suomi NPP) spacecraft were downloaded from NASA-FIRMS (Fire Information for Resource Management System) (NASA FIRMS, 2024). VIIRS Corrected Reflectance (True Color) imagery was downloaded from NASA-FIRMS (Lin and Wolfe, 2022a, b; NASA VIIRS Characterization Support Team (VCST)/ MODIS Adaptive Processing System (MODAPS), 2022a, b). The Ozone Mapping and Profiling Suite (OMPS) Aerosol Index overlay was downloaded from NASA-FIRMS (Torres and Goddard Earth Sciences Data and Information Services Center (GES DISC), 2019).

212 3 Results and Discussion

3.1 Breakdown of points flagged for each area

Figure 4A breaks down the percentage of points flagged for BB for each flight and for each location, with a breakdown based on cities in Fig 4B. Very little BB-influence was observed in the Philippines, with most of it occurring north of Manila under 1.5 km above ground level (AGL) (Fig S1). For Korea, the highest occurrences of BB occurred on flights 2 and 3. On flight 2 the majority of the BB was observed over the West Sea under 500 m AGL. For flight 3 there was BB-influence over both the West Sea and Seoul above 1 km AGL (Fig S2). Most of the observed BB-influence for the campaign occurred in Thailand, specifically flights 1 and 2, with Chiang Mai experiencing more BB compared to Bangkok (Fig S3), except for flight 3. Section 3.2 delves more into the geographical and temporal BB flag differences observed in Thailand during the campaign. Taiwan had the next highest percent occurrence, but Korea overall had more points flagged for BB compared to Taiwan. The total time spent collecting data over these locations is the reason for this discrepancy, the campaign spent almost four times as much time over Korea compared to Taiwan. However, in terms of cities, Kaohsiung had the third highest percentage and number of points flagged, after Chiang Mai and Bangkok, with most of these flagged points occurring on flight 1. Most of the BB observed in Taiwan occurred during the third flight, with the majority occurring on parts of the flight track not over Kaohsiung and above 1 km AGL (Fig S4).

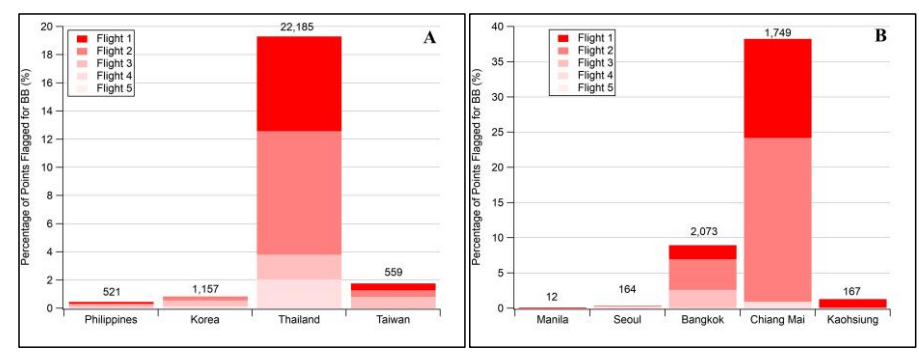


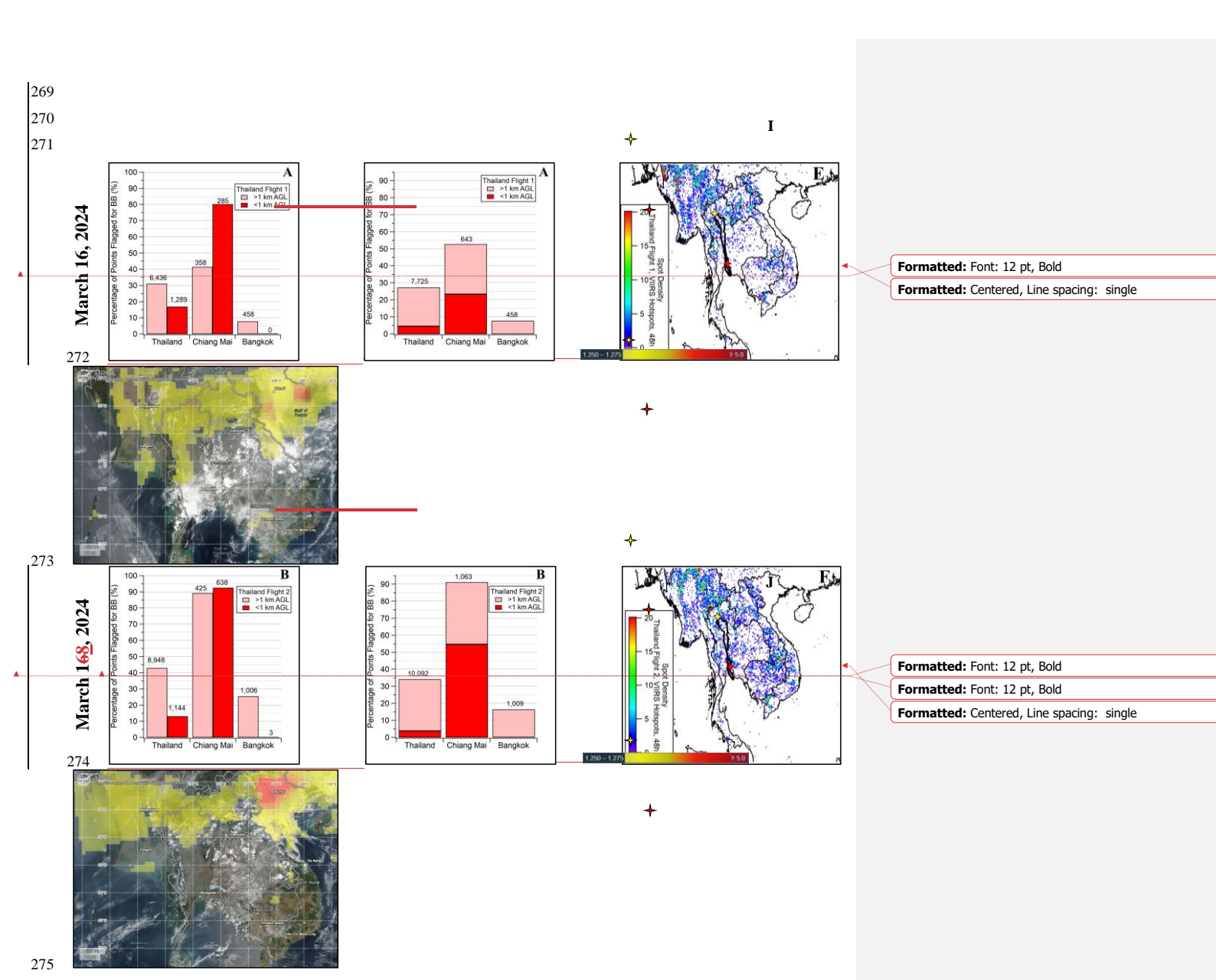
Figure 4. Percentage of points flagged for BB for each flight over each country (A) and select cities (B) with total number of points flagged displayed.

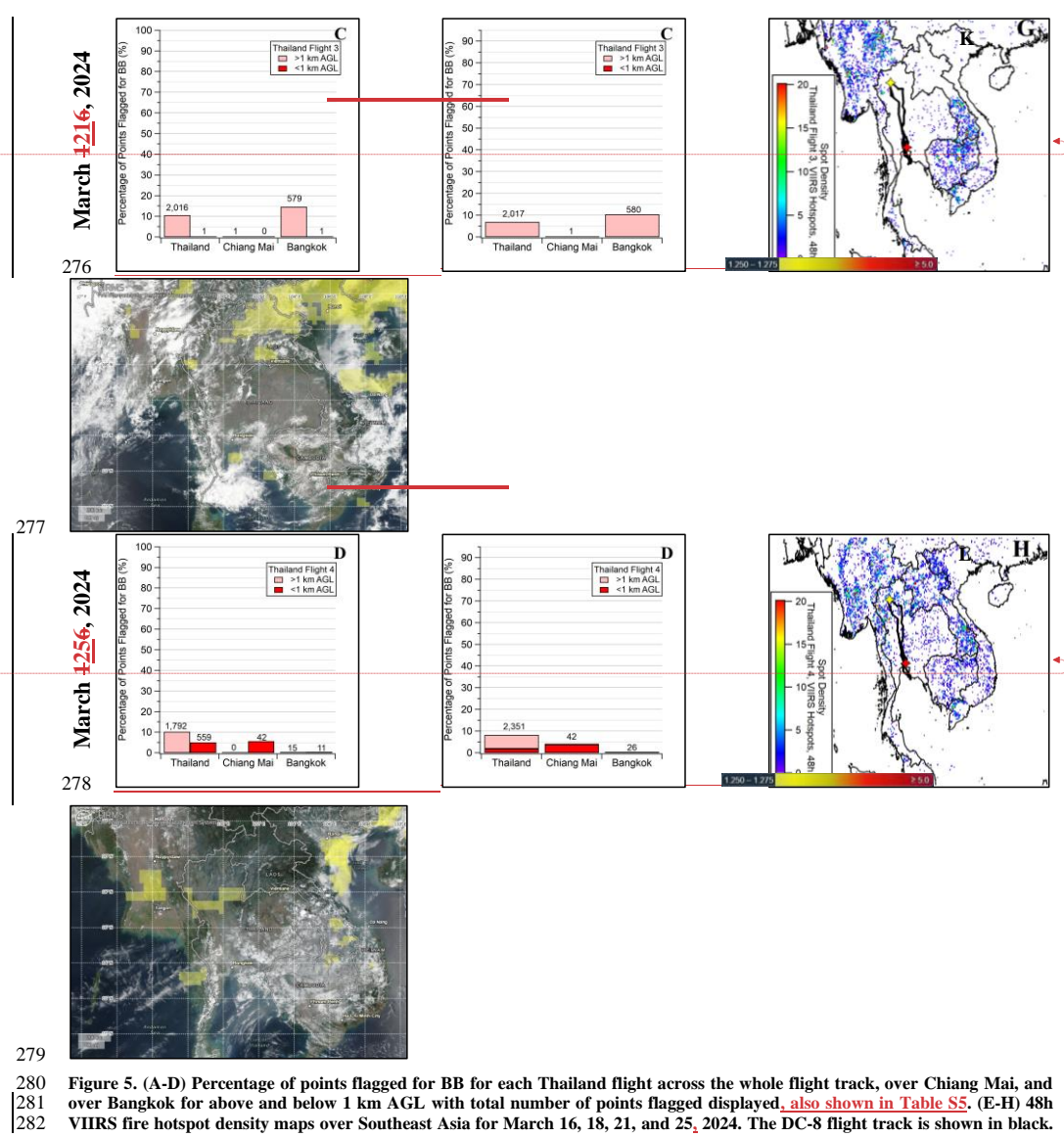
231 3.2 Thailand Case-Study

232 3.2.1 Flight by Flight Breakdown

233 Since Thailand had the largest prevalence of biomass burning among the flight locations, we have broken down these flights 234 in greater detail. Figure 5 shows the flight-by-flight breakdown of the BB flag (A-D), VIIRS 48h fire hotspot density maps (E-

H) and VIIRS satellite imagery with the OMPS aerosol index overlay (I-L) for the four Thailand flights. While flight 2 had 236 the highest overall occurrence of BB (10,092 points compared to 7,725) (Fig 5B), flight 1 had more BB-influence closer to the 237 surface (1,289 compared to 1,144) (Fig 5A). An increase in fire hotspot density is is also observed when comparing Fig 5E to 238 5F, where the density has increased in Eastern Thailand, Cambodia, and Northern Thailand/Myanmar. However, a similar 239 increase is not observed looking at the OMPS aerosol index overlays (Fig 5I to Fig 5J). For flight 1 (Fig 5I) the aerosol index 240 wais elevated over northern Laos, northern Vietnam, northern and western Thailand, and central and eastern Myanmar, 241 indicating either a more concentrated, thicker and/or higher layer of absorbing aerosols (dust and smoke) in these areas. For 242 flight 2 (Fig 5J) the higher aerosol index values are were concentrated over Hanoi, with western Thailand clearing up and few elevated values over eastern Thailand, Cambodia, and southern Laos. This apparent aerosol index decrease around Thailand 243 244 contrasts with what was observed using the BB flag and the VIIRS fire hotspot density maps, however, the OMPS aerosol index is also sensitive to changes in aerosol height, concentration, and degree of absorption (Torres and Goddard Earth 245 246 Sciences Data and Information Services Center (GES DISC), 2019). Prior to flight 3, the area received a considerable amount 247 of rain (~41 mm in Bangkok and up to 82 mm on the northern flight track on the day before flight 3), which likely washed out most of the smoke and put out local fires, seen in the decreased fire hotspot density across Thailand (Fig 5G), and decreased 248 249 aerosol indices (Fig 5K). For the final flight, there was's a slight increase in the number of points flagged compared to flight 3 (~17%), more near the surface as burning resumed, which is apparent when comparing the VIIRS fire hotspot density maps 250 251 (Fig 5G and Fig 5H) and scattered elevated aerosol indices over northern Thailand (Fig 5L). 252 Figure 5A-D also shows a breakdown of BB-influence in terms of major population centers on the flight track, specifically 253 Bangkok on the southern portion of the track and Chiang Mai on the northern part. For flight 1, we observed no BB-influence 254 was observed below 1 km in Bangkok across four low passes. This contrasts with observations during one pass in Chiang Mai 255 where ~80% of the low altitude data was were flagged for BB. This is consistent with Fig 5E, where the fire hot spot densities 256 are were higher around Chiang Mai compared to Bangkok, and Fig 5I with elevated aerosol indices over Chiang Mai. For 257 flight 2, there wereas equivalent amounts of BB-influence over the two cities, but significantly more at the surface in Chiang 258 Mai, however, relative to the time spent at each location over 90% of high-level data from Chiang Mai were flagged while 259 only ~1625% of high-level Bangkok data were. Even though the fire hotspot density around Bangkok wais higher for flight 2 260 (Fig 5F) compared to flight 1 (Fig 5E), that BB-influence does not appear to be have reaching reached the surface. One possible 261 explanation is that the prevailing southerly winds are-were blowing that smoke more towards Central Thailand. In the third flight, the rain likely washed out almost all of the smoke around Chiang Mai and quelled many fires as observed in Fig 5G. 262 263 However, there was still some BB-influence observed above Bangkok, perhaps by a transported airmass aloft unaffected by 264 the rain. From Fig 5G, there are-were still high fire hotspot densities occurring in Cambodia and Laos, which could be traced 265 forward to Bangkok using HysplitHYSPLIT back-trajectories (Fig 6A). For the last flight, there was little BB-influence 266 observed in both cities (<4~1% total) but still a meaningful amount across the rest of the flight track (~8%). Figure 5H shows 267 that fire activities seemed to have resumed throughout Thailand in the 48 hours leading up to flight 4.





Formatted: Font: 12 pt, Bold

Formatted: Centered, Line spacing: single

Formatted: Font: 12 pt, Bold

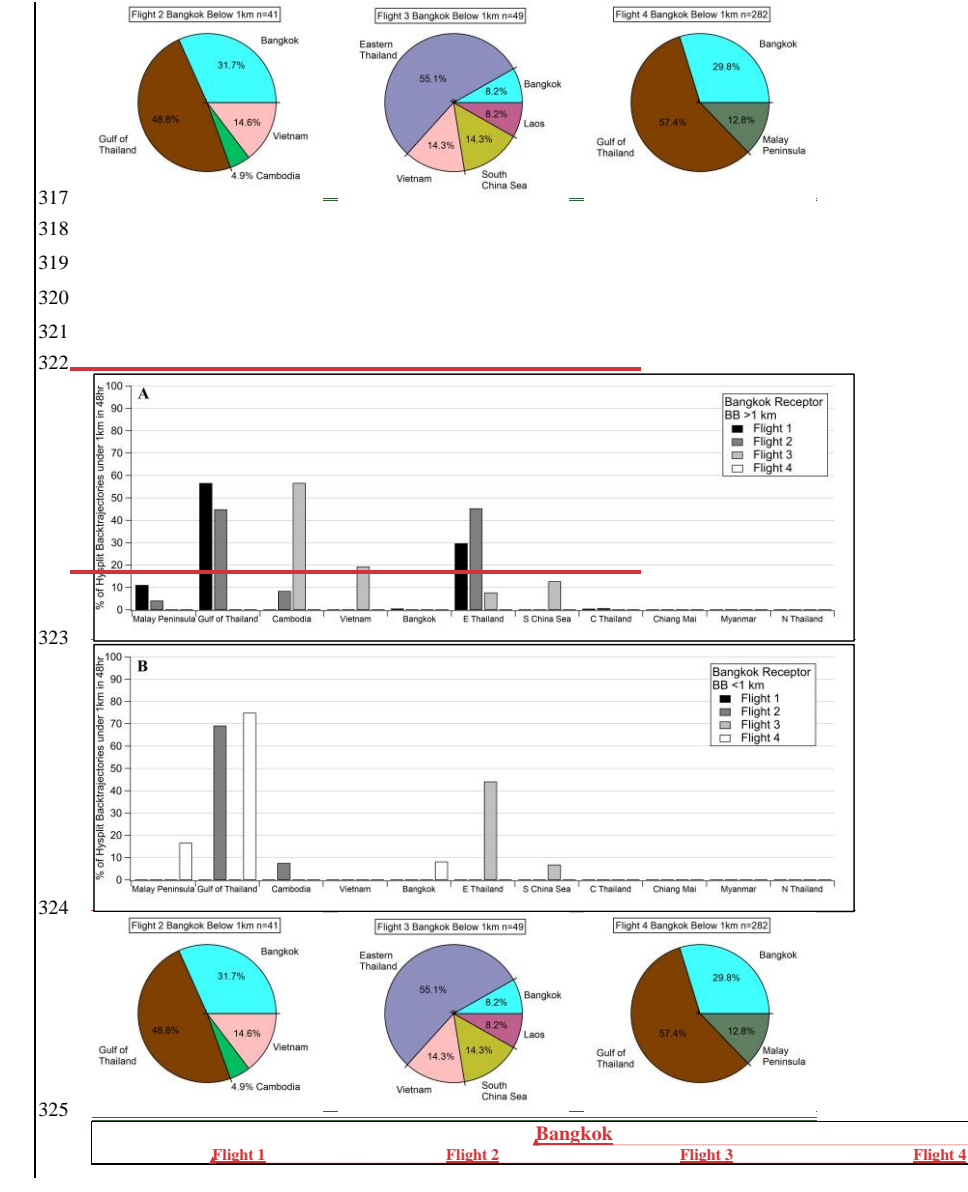
Formatted: Centered, Line spacing: single

Figure 5. (A-D) Percentage of points flagged for BB for each Thailand flight across the whole flight track, over Chiang Mai, and over Bangkok for above and below 1 km AGL with total number of points flagged displayed, also shown in Table S5. (E-H) 48h VIIRS fire hotspot density maps over Southeast Asia for March 16, 18, 21, and 25, 2024. The DC-8 flight track is shown in black.

The yellow star represents Chiang Mai, and the red star represents Bangkok. (I-L) VIIRS Corrected Reflectance (True Color) imagery with OMPS Aerosol Index overlay over Southeast Asia for March 16, 18, 21, and 25, 2024.

3.2.3 Air Mass Origin Breakdown

To better understand the air mass history at these locations, we used HysplitHYSPLIT back trajectory back trajectory modeling along the flight path to determine where these air masses came from and traveled through (using criteria from Table S4). Backtrajectories with an altitude < 1 km were then quantified over certain areas of interest for portions of the flight track that passed over Chiang Mai and Bangkok and were flagged for BB. Figure 6 shows the results for Bangkok for all of the flights above and below 1 km of altitude. For the first two Bangkok flights, there was influence from the south (Gulf of Thailand and Malay Peninsula) and northeast (Eastern Thailand) above 1 km altitude, which switched to the east (Cambodia and Vietnam) for flight 3. Under 1 km altitude for Bangkok flights 2 and 4, most of the BB was local or traveled from the south, while for flight 3 BB was transported from the northeast (Eastern Thailand and South China Sea). However, it should be noted that Bangkok experienced <0.5% of BB-flagged data for Flight 4 (Fig 5D) so these results are mostly likely reflective of a single plume. Fig. 7 shows the HysplitHYSPLIT back-trajectory back trajectory quantifications for Chiang Mai. For Chiang Mai above 1 km of altitude, the majority of back- trajectories are either from Central Thailand or Myanmar, with flight 1 dominated by BB transported from Central Thailand and flight 2 by Myanmar. Under 1 km altitude, there is a similar trend with flight 1 flagged back-trajectories originating from south of Chiang Mai and flight 2 and 4 from the west. These results are in agreement with satellite fire hotspot retrievals (Fig. 5E-H), that show the highest hotspot density around and northwest of Chiang Mai for flights 1, 2, and 4 but for flight 3 (Fig 5G) a clearer area around Chiang Mai. Additional areas of high fire hotspot density occurred in Cambodia, Vietnam, and Laos, especially in the last three flights.



Formatted: Font: 10 pt
Formatted Table
Formatted: Font: 8 pt

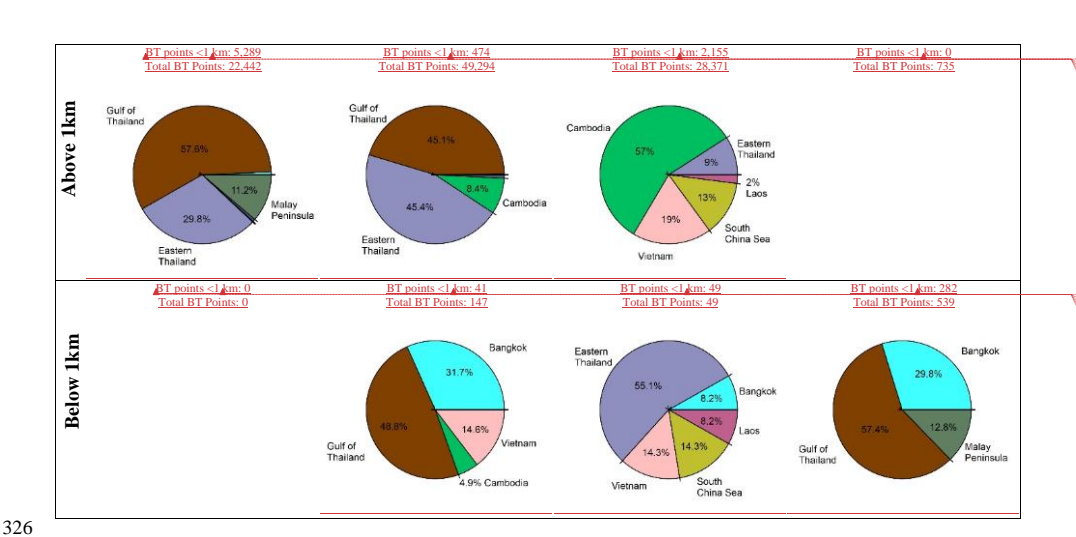
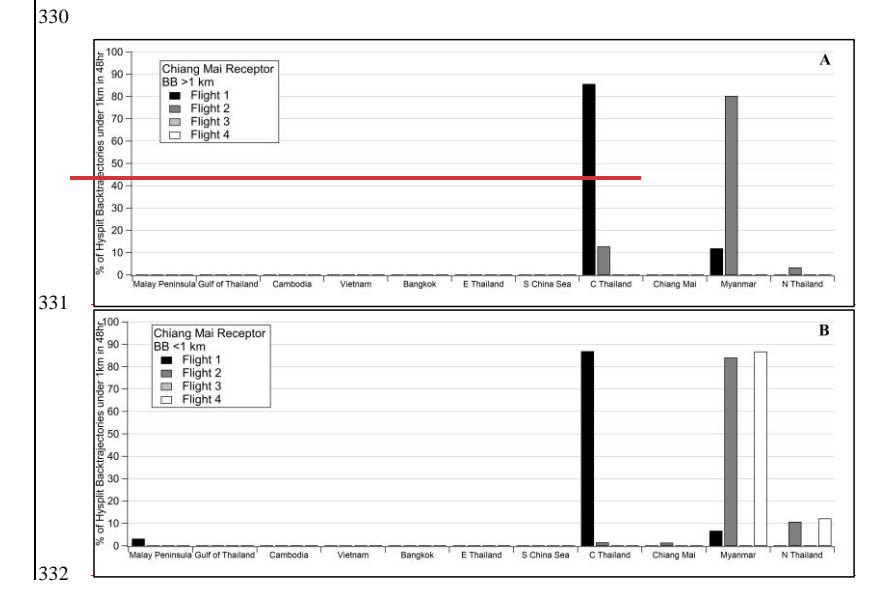
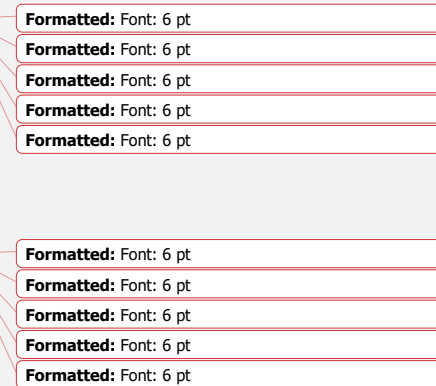


Figure 6. Hysplit HYSPLIT back-trajectoryback trajectory (BT) quantification for BB-flagged data over Bangkok for all flights above (A) and below (B) 1 km AGL. The number of BT points under 1 km are shown for each category along with the total number of BT points.





Formatted: Normal

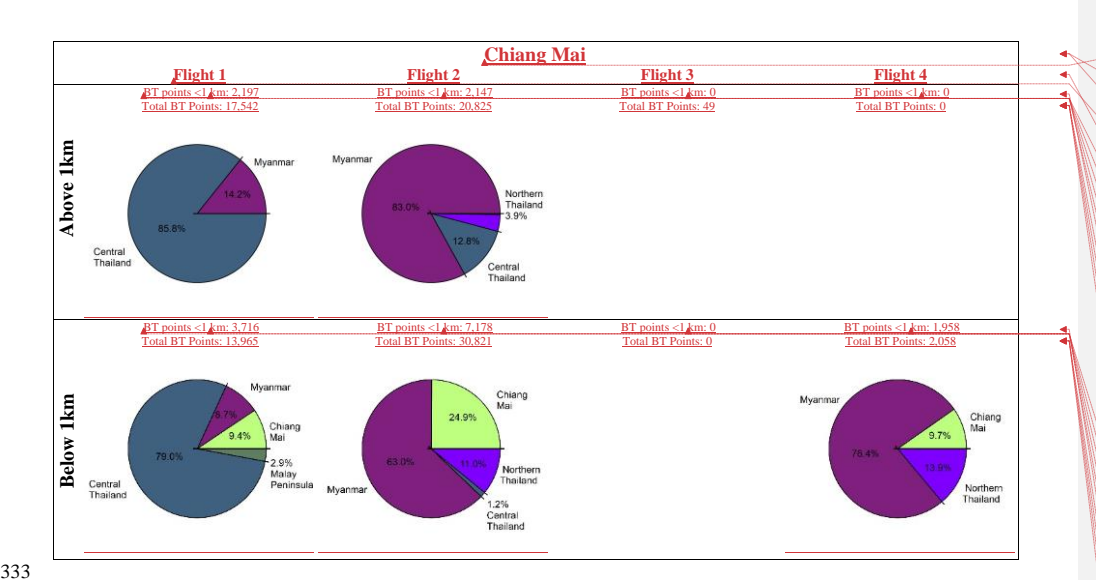


Figure 7. HysplitHYSPLIT back-trajectoryback trajectory (BT) quantification for BB-flagged data over Chiang Mai for all flights above (A) and below (B)-1 km AGL. The number of BT points under 1 km are shown for each category along with the total number of BT points.

3.2.4 Comparison of Microphysical Aerosol Characteristics

334

335

336

337

338

339

340

341

342

343

344 345

346 347

348349

350 351 To further illustrate the utility of the BB flag we have used it to compare the integrated size distribution of submicron aerosol particles. Figure 8A shows particle size distributions for BB-flagged data under 1 km in Chiang Mai and unflagged data under 1 km in Bangkok for the same day (flight 2). The BB-flagged data has a unimodal size distribution with a mean particle diameter of 150 nm (accumulation mode) compared to a bimodal size distribution in the unflagged data with a mean particle diameter 27 nm (nuclei mode). The second and less significant peak in the unflagged accumulation mode (mean diameter 136 nm) data may be the result of background BB presence, demonstrating that this flag is optimized for clear biomass burning influence and may overlook less obvious BB-influence. Several studies have demonstrated that aerosol size distributions in fresh (<1 h) smoke will start at median diameters ranging from 40-150 nm and grow to larger sizes with a decrease in modal width as they age (Hodshire et al., 2021; Janhäll et al., 2010; Reid et al., 1998). Figure 8B demonstrates a comparison between the same location (Chiang Mai <1 km) but on flights with differing amounts of BB-influence, i.e. flights 2 and 3. While the flight 3 unflagged data still exhibits smaller particle diameters (mean particle diameter 41 nm) than the flight 2 BB-flagged data (mean particle diameter 150 nm), it demonstrates a relatively stronger bimodal distribution compared to flight 2 unflagged data, with a mean particle diameter of 132 nm in the accumulation mode. Even though the presence of this accumulation mode

Formatted: Font: 10 pt Formatted: Indent: Left: -0.02" **Formatted Table** Formatted: Font: 8 pt Formatted: Indent: Left: -0.02" Formatted: Font: 6 pt Formatted: Indent: Left: -0.02" Formatted: Font: 6 pt Formatted: Indent: Left: -0.02" Formatted: Indent: Left: -0.02" Formatted: Indent: Left: Formatted: Indent: Left: -0.02" Formatted: Indent: Left: -0.02" 352 peak and BB markers (CO, HCN, and CH₃CN) within 20% of their respective thresholds indicates an influence from BB, the 353 dominant nuclei mode peak and $\Delta CO/\Delta CO_2$ (0.38%) and $\Delta CH_4/\Delta CO$ (104%) slopes point to urban combustion sources as the 354 dominant influence for this unflagged data. 355 When looking at black carbon mass concentrations, shown in Fig 9A, the BB-flagged data has consistently higher BC 356 concentrations compared to unflagged data across Thailand for flights 1 and 2. Flights 3 and 4 had the lowest BB-flagged BC 357 concentrations and were higher compared to the unflagged data but were within one standard deviation. This is consistent with Fig 5C and 5D where flights 3 and 4 had the smallest number of points flagged for BB. The unflagged BC concentrations for 358 flights 1, 2, and 4 are also higher than unflagged flight 3 (but within one standard deviation); therefore, assuming other BC 359 emissions are consistent between the flight days, this is further evidence that the BB flag does not capture all BB-influenced 360 361 data, specifically BB-influence in the background. Figure 9B shows that the non-volatile number fraction of fine particles for BB-flagged data is enhanced, with a narrower range compared to unflagged data across all four flights. One explanation may 362 363 be that the increased BC mass concentration is elevating the non-volatile number concentration of BB-flagged data in 364 combination with a decrease in the number concentration of volatile fine particles due to evaporation during transport. Future work examining the age of the smoke using short-lived BB tracers could provide more information on the concentration of 365

volatile fine particles in fresh and aged smoke plumes.

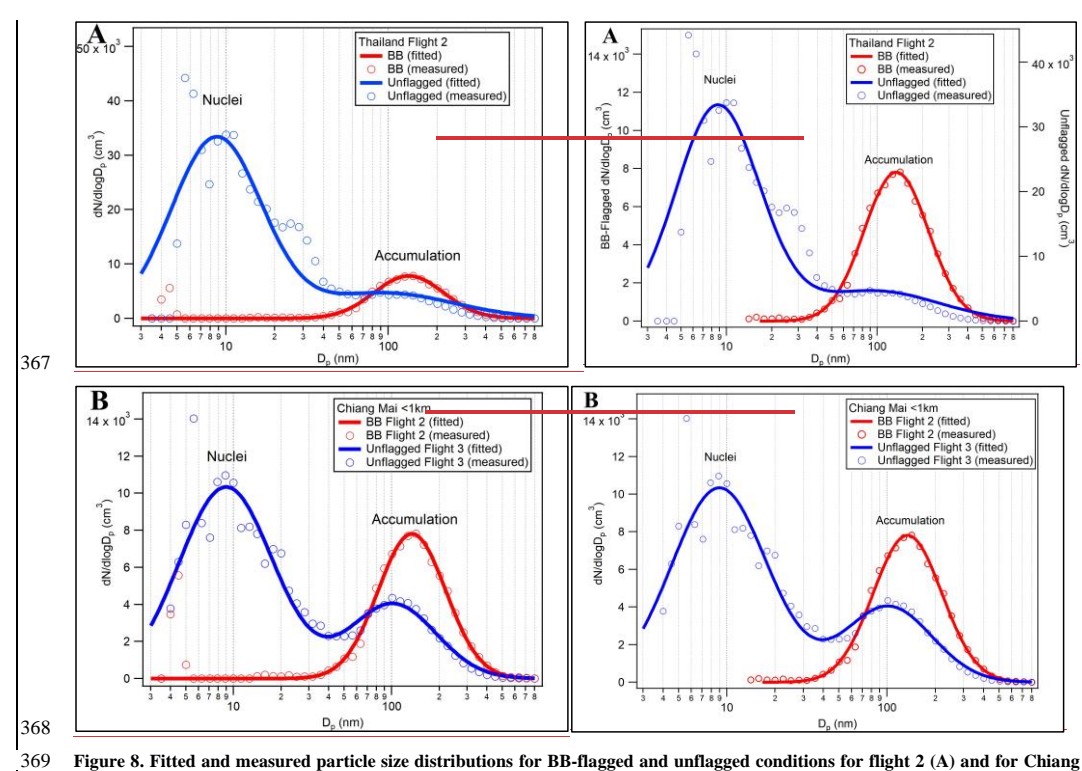
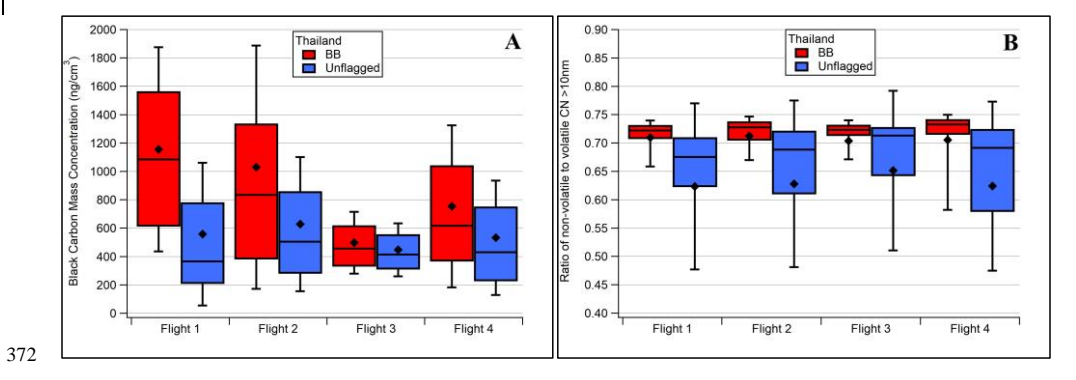


Figure 8. Fitted and measured particle size distributions for BB-flagged and unflagged conditions for flight 2 (A) and for Chiang Mai (B) < 1 km AGL. It should also be noted that the BB-flagged and unflagged distributions in 8A are on different scales but the same scale in 8B.



- 73 Figure 9. Black carbon mass concentrations (A) and non-volatile number fraction CN > 10 nm (B) for BB-flagged and unflagged
- 374 data for each Thailand flight. Whiskers are representative of one standard deviation, while the boxes represent the interquartile
- 375 range, the horizontal line the median, and the diamond the mean.

376 4 Conclusions

- 377 Biomass burning and inefficient combustion contribute to poor air quality and greenhouse gas emissions across the globe.
- 378 Airborne investigations in regions prone to these emissions provide more detailed and focused measurements than typical
- 379 ground or satellite methods. This work demonstrated a novel approach for identifying biomass burning-impacted airmasses in
- 380 an airborne dataset. A combination of biomass burning tracers and indicators were used to distinguish biomass burning-
- 381 impacted airmasses along each given flight track. The Thailand case study demonstrates the efficacy of this flag in determining
- areas most influenced by biomass burning and in combination with trajectory models, an idea of air mass history. Additionally,
- 383 a preliminary analysis of physical characteristics of aerosols revealed differences between BB-flagged and unflagged
- 384 airmasses, including aerosol size distributions, black carbon concentrations, and non-volatile number fraction. These findings,
- 385 while applicable to Asia, demonstrate the value of the method, which can be applied to other field campaigns with similar
- 386 measurements. The utility of the BB flag can be increased in the future with the use of specific volatile organic compounds
- 387 (VOCs) to provide information on the age of the smoke, e.g., primary BB VOCs versus secondary BB VOCs (Liang et al.,
- 388 2022). Additional development of a boundary layer flag for the ASIA-AQ dataset will improve future work studying the health
- 389 impacts of biomass burning smoke and inefficient combustion at ground level and transport in aloft layers.

390 Data Availability

391 All data used in this publication are open access and can found in the ASIA-AQ Data Archive

Archive

- 392 (https://doi.org/10.5067/SUBORBITAL/ASIA-AQ/DATA001), the FIRMS
- 393 (https://firms.modaps.eosdis.nasa.gov/download/), and the HYSPLITHYSPLIT model is available a
- 394 https://www.ready.noaa.gov/HYSPLITHYSPLIT.php.

395 Author Contribution

- 396 JAM, JPD, GSD, YC, RHM, LDZ, FG, CEJ, MS, EBW, ELW, SR, YRL, KB, JDC, PW, FP, SS, WW, and AW participated
- 397 in the data collection. JAM, JPD, GSD, MS, FG, KB, and WW performed the data analysis and provided feedback. JAM
- 398 prepared the manuscript with contributions from all coauthors.

Competing Interests

399

400 The contact author has declared that none of the authors have any competing interests.

401 Acknowledgments

- 402 The authors would like to thank Jim Crawford and the entire ASIA-AQ leadership team for their support, guidance, and
- 403 feedback. The authors thank NASA's Earth Science Project Office for their logistical support collecting this data. We thank
- 404 Ryan Bennett, David Van Gilst, and Terry Hu for aircraft navigational and meteorological data. The authors thank Dave
- 405 Eckberg and Mauro Rana for their software and hardware support with the DACOM-DLH instrumentation. Jason Miech's
- 406 research was supported by an appointment to the NASA Postdoctoral Program at the NASA Langley Research Center,
- 407 administered by Oak Ridge Associated Universities under contract with NASA. Data collection was funded by the ASIA-AO
- 408 project under NASA's Tropospheric Composition Program. PTR-ToF-MS measurements aboard the NASA DC-8 during
- 409 ASIA-AO were partially funded by the Austrian Federal Ministry for Climate Action, Environment, Energy, Mobility,
- 410 Innovation, and Technology (BMK), represented by the Austrian Research Promotion Agency (FFG), through the Austrian
- $411 \quad Space \ Applications \ Programme \ (ASAP\ 2022, \#FO999900547). \ IONICON\ Analytik \ is \ acknowledged \ for \ supplying \ a \ FUSION$
- 412 PTR-ToF-MS analyzer and providing staff support. The authors gratefully acknowledge the NOAA Air Resources Laboratory
- 413 (ARL) for the provision of the HYSPLITHYSPLIT transport and dispersion model and/or READY website
- 414 (https://www.ready.noaa.gov) used in this publication. We acknowledge the use of data and/or imagery from NASA's Land,
- 415 Atmosphere Near real-time Capability for Earth observations (LANCE) (https://earthdata.nasa.gov/lance), part of NASA's
- 416 Earth Science Data and Information System (ESDIS). We acknowledge the use of data and/or imagery from NASA's Fire
- 417 Information for Resource Management System (FIRMS) (https://www.earthdata.nasa.gov/data/tools/firms), part of NASA's
- 418 Earth Science Data and Information System (ESDIS).

419 References

- 420 Akagi, S. K., Yokelson, R. J., Wiedinmyer, C., Alvarado, M. J., Reid, J. S., Karl, T., Crounse, J. D., and Wennberg, P. O.:
- 421 Emission factors for open and domestic biomass burning for use in atmospheric models, Atmospheric Chemistry and Physics,
- 422 11, 4039–4072, https://doi.org/10.5194/acp-11-4039-2011, 2011.
- 423 Anderson, T. L. and Ogren, J. A.: Determining Aerosol Radiative Properties Using the TSI 3563 Integrating Nephelometer,
- 424 Aerosol Science and Technology, 29, 57–69, https://doi.org/10.1080/02786829808965551, 1998.
- 425 Andreae, M. O. and Merlet, P.: Emission of trace gases and aerosols from biomass burning, Global Biogeochemical Cycles,
- 426 15, 955–966, https://doi.org/10.1029/2000GB001382, 2001.
- 427 ASIA-AO Science Team: ASIA-AO Field Campaign Data, https://doi.org/doi.org/10.5067/SUBORBITAL/ASIA-
- 428 AQ/DATA001, 2024.
- 429 Cambaliza, M. O. L., Shepson, P. B., Bogner, J., Caulton, D. R., Stirm, B., Sweeney, C., Montzka, S. A., Gurney, K. R.,
- 430 Spokas, K., Salmon, O. E., Lavoie, T. N., Hendricks, A., Mays, K., Turnbull, J., Miller, B. R., Lauvaux, T., Davis, K., Karion,
- 431 A., Moser, B., Miller, C., Obermeyer, C., Whetstone, J., Prasad, K., Miles, N., and Richardson, S.: Quantification and source
- 432 apportionment of the methane emission flux from the city of Indianapolis, Elementa: Science of the Anthropocene, 3, 000037,
- 433 https://doi.org/10.12952/journal.elementa.000037, 2015.

- 434 Cantrell, C. A.: Technical Note: Review of methods for linear least-squares fitting of data and application to atmospheric
- 435 chemistry problems, Atmospheric Chemistry and Physics, 8, 5477-5487, https://doi.org/10.5194/acp-8-5477-2008, 2008.
- 436 Crounse, J. D., McKinney, K. A., Kwan, A. J., and Wennberg, P. O.: Measurement of Gas-Phase Hydroperoxides by Chemical
- 437 Ionization Mass Spectrometry, Analytical Chemistry, 78, 6726–6732, https://doi.org/10.1021/ac0604235, 2006.
- 438 DiGangi, J. P., Choi, Y., Nowak, J. B., Halliday, H. S., Diskin, G. S., Feng, S., Barkley, Z. R., Lauvaux, T., Pal, S., Davis, K.
- 439 J., Baier, B. C., and Sweeney, C.: Seasonal Variability in Local Carbon Dioxide Biomass Burning Sources Over Central and
- 440 Eastern US Using Airborne In Situ Enhancement Ratios, Journal of Geophysical Research: Atmospheres, 126,
- 441 e2020JD034525, https://doi.org/10.1029/2020JD034525, 2021.
- 442 DiGangi, J. P., Diskin, G. S., Yoon, S., Alvarez, S. L., Flynn, J. H., Robinson, C. E., Shook, M. A., Thornhill, K. L., Winstead,
- 443 E. L., Ziemba, L. D., Cambaliza, M. O. L., Simpas, J. B., Hilario, M. R. A., and Sorooshian, A.: Technical note: Apportionment
- 444 of Southeast Asian Biomass Burning and Urban Influence via In Situ Trace Gas Enhancement Ratios, EGUsphere, 2025, 1-
- 445 16, https://doi.org/10.5194/egusphere-2025-1454, 2025.
- 446 Draxler, R. R.: HYSPLITHYSPLIT 4 User's Guide. NOAA technical memorandum ERL ARL-230, 1999.
- 447 Draxler, R. R. and Hess, G. D.: Description of the HYSPLITHYSPLIT4 modeling system, NOAA technical memorandum
- 448 ERL ARL-224, 1997.
- 449 Draxler, R. R. and Hess, G. D.: An overview of the HYSPLITHYSPLIT_4 modelling system for trajectories, Australian
- 450 meteorological magazine, 47, 295-308, 1998.
- 451 Fiehn, A., Eckl, M., Kostinek, J., Gałkowski, M., Gerbig, C., Rothe, M., Röckmann, T., Menoud, M., Maazallahi, H., Schmidt,
- 452 M., Korbeń, P., Neçki, J., Stanisavljević, M., Swolkień, J., Fix, A., and Roiger, A.: Source apportionment of methane emissions
- 453 from the Upper Silesian Coal Basin using isotopic signatures, Atmospheric Chemistry and Physics, 23, 15749–15765,
- 454 https://doi.org/10.5194/acp-23-15749-2023, 2023.
- 455 Guha, A., Gentner, D. R., Weber, R. J., Provencal, R., and Goldstein, A. H.: Source apportionment of methane and nitrous
- 456 oxide in California's San Joaquin Valley at CalNex 2010 via positive matrix factorization, Atmospheric Chemistry and
- 457 Physics, 15, 12043–12063, https://doi.org/10.5194/acp-15-12043-2015, 2015.
- 458 Halliday, H. S., DiGangi, J. P., Choi, Y., Diskin, G. S., Pusede, S. E., Rana, M., Nowak, J. B., Knote, C., Ren, X., He, H.,
- 459 Dickerson, R. R., and Li, Z.: Using Short-Term CO/CO2 Ratios to Assess Air Mass Differences Over the Korean Peninsula
- 460 During KORUS-AQ, Journal of Geophysical Research: Atmospheres, 124, 10951-10972,
- 461 https://doi.org/10.1029/2018JD029697, 2019.
- 462 Helfter, C., Tremper, A. H., Halios, C. H., Kotthaus, S., Bjorkegren, A., Grimmond, C. S. B., Barlow, J. F., and Nemitz, E.:
- 463 Spatial and temporal variability of urban fluxes of methane, carbon monoxide and carbon dioxide above London, UK,
- 464 Atmospheric Chemistry and Physics, 16, 10543–10557, https://doi.org/10.5194/acp-16-10543-2016, 2016.
- 465 Hodshire, A. L., Ramnarine, E., Akherati, A., Alvarado, M. L., Farmer, D. K., Jathar, S. H., Kreidenweis, S. M., Lonsdale, C.
- 466 R., Onasch, T. B., Springston, S. R., Wang, J., Wang, Y., Kleinman, L. I., Sedlacek III, A. J., and Pierce, J. R.: Dilution impacts
- on smoke aging: evidence in Biomass Burning Observation Project (BBOP) data, Atmospheric Chemistry and Physics, 21,
- 468 6839–6855, https://doi.org/10.5194/acp-21-6839-2021, 2021.
- 469 Holzinger, R., Warneke, C., Hansel, A., Jordan, A., Lindinger, W., Scharffe, D. H., Schade, G., and Crutzen, P. J.: Biomass
- 470 burning as a source of formaldehyde, acetaldehyde, methanol, acetone, acetonitrile, and hydrogen cyanide, Geophysical
- 471 Research Letters, 26, 1161–1164, https://doi.org/10.1029/1999GL900156, 1999.

- 472 Huangfu, Y., Yuan, B., Wang, S., Wu, C., He, X., Qi, J., de Gouw, J., Warneke, C., Gilman, J. B., Wisthaler, A., Karl, T.,
- 473 Graus, M., Jobson, B. T., and Shao, M.: Revisiting Acetonitrile as Tracer of Biomass Burning in Anthropogenic-Influenced
- 474 Environments, Geophysical Research Letters, 48, e2020GL092322, https://doi.org/10.1029/2020GL092322, 2021.
- 475 Janhäll, S., Andreae, M. O., and Pöschl, U.: Biomass burning aerosol emissions from vegetation fires: particle number and
- 476 mass emission factors and size distributions, Atmospheric Chemistry and Physics, 10, 1427–1439, https://doi.org/10.5194/acp-
 - 77 10-1427-2010, 2010.
- 478 Kurokawa, J. and Ohara, T.: Long-term historical trends in air pollutant emissions in Asia: Regional Emission inventory in
- 479 ASia (REAS) version 3, Atmospheric Chemistry and Physics, 20, 12761–12793, https://doi.org/10.5194/acp-20-12761-2020,
- 480 2020.
- 481 Kurokawa, J., Ohara, T., Morikawa, T., Hanayama, S., Janssens-Maenhout, G., Fukui, T., Kawashima, K., and Akimoto, H.:
- 482 Emissions of air pollutants and greenhouse gases over Asian regions during 2000–2008: Regional Emission inventory in ASia
- 483 (REAS) version 2, Atmospheric Chemistry and Physics, 13, 11019–11058, https://doi.org/10.5194/acp-13-11019-2013, 2013.
- 484 Liang, Y., Weber, R. J., Misztal, P. K., Jen, C. N., and Goldstein, A. H.: Aging of Volatile Organic Compounds in October
- 485 2017 Northern California Wildfire Plumes, Environ. Sci. Technol., 56, 1557–1567, https://doi.org/10.1021/acs.est.1c05684,
- 486 2022.

499

- 487 Lin, G. and Wolfe, R.: VIIRS/NPP Imagery Resolution Terrain-Corrected Geolocation L1 6-Min Swath 375m NRT,
- 488 https://doi.org/10.5067/VIIRS/VNP03IMG_NRT.002, 2022a.
- 489 Lin, G. and Wolfe, R.: VIIRS/NPP Moderate Resolution Terrain-Corrected Geolocation L1 6-Min Swath 750m NRT,
- 490 https://doi.org/10.5067/VIIRS/VNP03MOD_NRT.002, 2022b.
- 1470 https://doi.org/10.500// VINCS/ VINCS/
- 492 J. S., Reid, J. S., Lee, C.-T., Wang, L.-C., Wang, J.-L., Hsu, C. N., Sayer, A. M., Holben, B. N., Chu, Y.-C., Nguyen, X. A.,

Lin, N.-H., Tsay, S.-C., Maring, H. B., Yen, M.-C., Sheu, G.-R., Wang, S.-H., Chi, K. H., Chuang, M.-T., Ou-Yang, C.-F., Fu,

- 492 J. S., Reid, J. S., Lee, C.-1., Wang, E.-C., Wang, J.-L., Hsu, C. N., Sayer, A. M., Holbert, B. N., Chu, T.-C., Nguyen, A. A., Sopajaree, K., Chen, S.-J., Cheng, M.-T., Tsuang, B.-J., Tsai, C.-J., Peng, C.-M., Schnell, R. C., Conway, T., Chang, C.-T.,
- 494 Lin, K.-S., Tsai, Y. I., Lee, W.-J., Chang, S.-C., Liu, J.-J., Chiang, W.-L., Huang, S.-J., Lin, T.-H., and Liu, G.-R.: An overview
- 495 of regional experiments on biomass burning aerosols and related pollutants in Southeast Asia: From BASE-ASIA and the
- 496 Dongsha Experiment to 7-SEAS, Atmospheric Environment, 78, 1–19, https://doi.org/10.1016/j.atmosenv.2013.04.066, 2013.
- 497 Lobert, J. M., Scharffe, D. H., Hao, W. M., and Crutzen, P. J.: Importance of biomass burning in the atmospheric budgets of
- 498 <u>nitrogen-containing gases</u>, Nature, 346, 552–554, https://doi.org/10.1038/346552a0, 1990.
- 500 Müller, M., Anderson, B. E., Beyersdorf, A. J., Crawford, J. H., Diskin, G. S., Eichler, P., Fried, A., Keutsch, F. N., Mikoviny,
- 501 T., Thornhill, K. L., Walega, J. G., Weinheimer, A. J., Yang, M., Yokelson, R. J., and Wisthaler, A.: In situ measurements and
- 502 modeling of reactive trace gases in a small biomass burning plume, Atmospheric Chemistry and Physics, 16, 3813-3824,
- 503 https://doi.org/10.5194/acp-16-3813-2016, 2016.
- 504 Nara, H., Tanimoto, H., Tohjima, Y., Mukai, H., Nojiri, Y., and Machida, T.: Emission factors of CO2, CO and CH4 from
- 505 Sumatran peatland fires in 2013 based on shipboard measurements, Tellus B: Chemical and Physical Meteorology, 69,
- 506 1399047, https://doi.org/10.1080/16000889.2017.1399047, 2017.
- 507 NASA FIRMS: NRT VIIRS 375 m Active Fire product VNP14IMGT,
- 508 https://doi.org/10.5067/FIRMS/VIIRS/VNP14IMGT_NRT.002, 2024.

Formatted: Default Paragraph Font

Formatted: Bibliography

Formatted: Default Paragraph Font

- 509 NASA VIIRS Characterization Support Team (VCST)/ MODIS Adaptive Processing System (MODAPS): VIIRS/NPP
- 510 Imagery Resolution 6-Min L1B Swath 375m NRT, https://doi.org/10.5067/VIIRS/VNP02IMG_NRT.002, 2022a.
- 511 NASA VIIRS Characterization Support Team (VCST)/ MODIS Adaptive Processing System (MODAPS): VIIRS/NPP
- 12 Moderate Resolution Bands L1B 6-Min Swath 750m NRT, https://doi.org/10.5067/VIIRS/VNP02MOD_NRT.002, 2022b.
- 513 Reid, J. S., Hobbs, P. V., Ferek, R. J., Blake, D. R., Martins, J. V., Dunlap, M. R., and Liousse, C.: Physical, chemical, and
- 514 optical properties of regional hazes dominated by smoke in Brazil, Journal of Geophysical Research: Atmospheres, 103,
- 15 32059–32080, https://doi.org/10.1029/98JD00458, 1998.
- 516 Reid, J. S., Maring, H. B., Narisma, G. T., van den Heever, S., Di Girolamo, L., Ferrare, R., Lawson, P., Mace, G. G., Simpas,
- J. B., Tanelli, S., Ziemba, L., van Diedenhoven, B., Bruintjes, R., Bucholtz, A., Cairns, B., Cambaliza, M. O., Chen, G., Diskin,
- 518 G. S., Flynn, J. H., Hostetler, C. A., Holz, R. E., Lang, T. J., Schmidt, K. S., Smith, G., Sorooshian, A., Thompson, E. J.,
 - 19 Thornhill, K. L., Trepte, C., Wang, J., Woods, S., Yoon, S., Alexandrov, M., Alvarez, S., Amiot, C. G., Bennett, J. R., Brooks,
- 520 M., Burton, S. P., Cayanan, E., Chen, H., Collow, A., Crosbie, E., DaSilva, A., DiGangi, J. P., Flagg, D. D., Freeman, S. W.,
- 521 Fu, D., Fukada, E., Hilario, M. R. A., Hong, Y., Hristova-Veleva, S. M., Kuehn, R., Kowch, R. S., Leung, G. R., Loveridge,
- 522 J., Meyer, K., Miller, R. M., Montes, M. J., Moum, J. N., Nenes, A., Nesbitt, S. W., Norgren, M., Nowottnick, E. P., Rauber,
- 523 R. M., Reid, E. A., Rutledge, S., Schlosser, J. S., Sekiyama, T. T., Shook, M. A., Sokolowsky, G. A., Stamnes, S. A., Tanaka,
- 524 T. Y., Wasilewski, A., Xian, P., Xiao, Q., Xu, Z., and Zavaleta, J.: The Coupling Between Tropical Meteorology, Aerosol
- 525 Lifecycle, Convection, and Radiation during the Cloud, Aerosol and Monsoon Processes Philippines Experiment (CAMP2Ex),
- 526 Bulletin of the American Meteorological Society, 104, E1179–E1205, https://doi.org/10.1175/BAMS-D-21-0285.1, 2023.
- 527 Reinecke, T., Leiminger, M., Jordan, A., Wisthaler, A., and Müller, M.: Ultrahigh Sensitivity PTR-MS Instrument with a Well-
- 528 Defined Ion Chemistry, Analytical Chemistry, 95, 11879–11884, https://doi.org/10.1021/acs.analchem.3c02669, 2023.
- 529 Sachse, G. W., Hill, G. F., Wade, L. O., and Perry, M. G.: Fast-response, high-precision carbon monoxide sensor using a
- 530 tunable diode laser absorption technique, Journal of Geophysical Research: Atmospheres, 92, 2071-2081,
- 31 https://doi.org/10.1029/JD092iD02p02071, 1987.
- 532 Sachse, G. W., Jr., J. E. C., Hill, G. F., Wade, L. O., Burney, L. G., and Ritter, J. A.: Airborne tunable diode laser sensor for
- 533 high-precision concentration and flux measurements of carbon monoxide and methane, in: Proc.SPIE, 157-166,
- 534 https://doi.org/10.1117/12.46162, 1991.
- 535 Schroeder, W., Oliva, P., Giglio, L., and Csiszar, I. A.: The New VIIRS 375m active fire detection data product: Algorithm
- 536 description and initial assessment. Remote Sensing of Environment. 143. 85–96. https://doi.org/10.1016/j.rse.2013.12.008.
- 537 2014.
- 538 Stein, A. F., Draxler, R. R., Rolph, G. D., Stunder, B. J. B., Cohen, M. D., and Ngan, F.: NOAA's HYSPLITHYSPLIT
- 539 Atmospheric Transport and Dispersion Modeling System, Bulletin of the American Meteorological Society, 96, 2059-2077,
- 540 https://doi.org/10.1175/BAMS-D-14-00110.1, 2015.
- 541 Torres, O. and Goddard Earth Sciences Data and Information Services Center (GES DISC): OMPS-NPP L2 NM Aerosol Index
- 542 swath orbital V2, https://doi.org/10.5067/40L92G8144IV, 2019.
- Tsay, S.-C., Hsu, N. C., Lau, W. K.-M., Li, C., Gabriel, P. M., Ji, Q., Holben, B. N., Judd Welton, E., Nguyen, A. X., Janjai,
- 544 S., Lin, N.-H., Reid, J. S., Boonjawat, J., Howell, S. G., Huebert, B. J., Fu, J. S., Hansell, R. A., Sayer, A. M., Gautam, R.,
- Wang, S.-H., Goodloe, C. S., Miko, L. R., Shu, P. K., Loftus, A. M., Huang, J., Kim, J. Y., Jeong, M.-J., and Pantina, P.: From
- 546 BASE-ASIA toward 7-SEAS: A satellite-surface perspective of boreal spring biomass-burning aerosols and clouds in
- 547 Southeast Asia, Atmospheric Environment, 78, 20–34, https://doi.org/10.1016/j.atmosenv.2012.12.013, 2013.

- 548 Vay, S. A., Woo, J.-H., Anderson, B. E., Thornhill, K. L., Blake, D. R., Westberg, D. J., Kiley, C. M., Avery, M. A., Sachse,
- 549 G. W., Streets, D. G., Tsutsumi, Y., and Nolf, S. R.: Influence of regional-scale anthropogenic emissions on CO2 distributions
- over the western North Pacific, Journal of Geophysical Research: Atmospheres, 108, https://doi.org/10.1029/2002JD003094,
- 551 2003.

- 552 Warneke, C., Schwarz, J. P., Dibb, J., Kalashnikova, O., Frost, G., Al-Saad, J., Brown, S. S., Brewer, Wm. A., Soja, A., Seidel,
- 553 F. C., Washenfelder, R. A., Wiggins, E. B., Moore, R. H., Anderson, B. E., Jordan, C., Yacovitch, T. I., Herndon, S. C., Liu,
- 554 S., Kuwayama, T., Jaffe, D., Johnston, N., Selimovic, V., Yokelson, R., Giles, D. M., Holben, B. N., Goloub, P., Popovici, I.,
- 555 Trainer, M., Kumar, A., Pierce, R. B., Fahey, D., Roberts, J., Gargulinski, E. M., Peterson, D. A., Ye, X., Thapa, L. H., Saide,
- 556 P. E., Fite, C. H., Holmes, C. D., Wang, S., Coggon, M. M., Decker, Z. C. J., Stockwell, C. E., Xu, L., Gkatzelis, G., Aikin,
- 557 K., Lefer, B., Kaspari, J., Griffin, D., Zeng, L., Weber, R., Hastings, M., Chai, J., Wolfe, G. M., Hanisco, T. F., Liao, J.,
- 558 Campuzano Jost, P., Guo, H., Jimenez, J. L., Crawford, J., and The FIREX-AQ Science Team: Fire Influence on Regional to
- 559 Global Environments and Air Quality (FIREX-AQ), Journal of Geophysical Research: Atmospheres, 128, e2022JD037758,
- 60 https://doi.org/10.1029/2022JD037758, 2023.
- 561 Yokelson, R. J., Griffith, D. W. T., and Ward, D. E.: Open-path Fourier transform infrared studies of large-scale laboratory
- 562 biomass fires, Journal of Geophysical Research: Atmospheres, 101, 21067–21080, https://doi.org/10.1029/96JD01800, 1996.
- 563 Yokelson, R. J., Crounse, J. D., DeCarlo, P. F., Karl, T., Urbanski, S., Atlas, E., Campos, T., Shinozuka, Y., Kapustin, V.,
- 564 Clarke, A. D., Weinheimer, A., Knapp, D. J., Montzka, D. D., Holloway, J., Weibring, P., Flocke, F., Zheng, W., Toohey, D.,
- 565 Wennberg, P. O., Wiedinmyer, C., Mauldin, L., Fried, A., Richter, D., Walega, J., Jimenez, J. L., Adachi, K., Buseck, P. R.,
- 566 Hall, S. R., and Shetter, R.: Emissions from biomass burning in the Yucatan, Atmospheric Chemistry and Physics, 9, 5785-
- 567 5812, https://doi.org/10.5194/acp-9-5785-2009, 2009.
- 568 Yokelson, R. J., Andreae, M. O., and Akagi, S. K.: Pitfalls with the use of enhancement ratios or normalized excess mixing
- 569 ratios measured in plumes to characterize pollution sources and aging, Atmospheric Measurement Techniques, 6, 2155–2158,
- 570 https://doi.org/10.5194/amt-6-2155-2013, 2013.
- 571 York, D., Evensen, N. M., Martínez, M. L., and De Basabe Delgado, J.: Unified equations for the slope, intercept, and standard
- 572 errors of the best straight line, American Journal of Physics, 72, 367–375, https://doi.org/10.1119/1.1632486, 2004.